Atmospheric
Chemistry
and Physics
Discussions

Long-range transport of volcanic aerosol from the 2010 Merapi tropical eruption to Antarctica

Xue Wu[1,2], Sabine Griessbach[1], Lars Hoffmann[1]

[1]Jülich Supercomputing Centre, Forschungszentrum Jülich, Jülich, Germany

[2]Key Laboratory of Middle Atmosphere and Global Environment Observation, Institute of Atmospheric Physics, Chinese Academy of Sciences, Beijing, China

Correspondence to: Xue Wu (xu.wu@fz-juelich.de)

Abstract

Volcanic sulfate aerosol is an important source of sulfur for Antarctica where other local sources of sulfur are rare. Mid- and high latitude volcanic eruptions can directly influence the aerosol budget of the polar stratosphere. However, tropical eruptions can also enhance polar aerosol load following long-range transport. In the present work, we analyze the volcanic plume of a tropical eruption, Mount Merapi in October 2010, using the Lagrangian particle dispersion model Massive-Parallel Trajectory Calculations (MPTRAC), Atmospheric Infrared Sounder (AIRS) SO_2 observations and Michelson Interferometer for Passive Atmospheric Sounding (MIPAS) aerosol observations. We investigate the pathway and transport efficiency of the volcanic aerosol from the tropical tropopause layer (TTL) to the lower stratosphere over Antarctica. We first estimated the time- and height-resolved SO_2 injection time series over Mount Merapi during the explosive eruption using the AIRS SO_2 observations and a backward trajectory approach. Then the SO_2 injections were tracked for up to 6 months using the MPTRAC model. The Lagrangian transport simulation of the volcanic plume was compared to MIPAS aerosol observations and showed good agreement. Both of the simulation and the observations presented in this study suggest that a significant amount of aerosols of the volcanic plume from the Merapi eruption was transported from the tropics to the south of 60°S within one month after the eruption and even further to Antarctica in the following two months. This relatively fast meridional transport of volcanic aerosol was mainly driven by quasi-horizontal mixing from the TTL to the extratropical lower stratosphere, which was facilitated by the weakening of the subtropical jet during the seasonal transition from austral spring to summer and linked to the westerly phase of the quasi-biennial oscillation (QBO). When the plume went to southern high latitudes, the polar vortex was displaced from the south pole, so the volcanic plume was carried to the south pole without penetrating the polar vortex. Based on the model results, the most efficient pathway for the quasi-horizontal mixing was in between the isentropic surfaces of 360 and 430 K. Although only 4% of the initial SO_2 load was transported into

Atmospheric
Chemistry
and Physics
Discussions

32   the lower stratosphere south of 60°S, the Merapi eruption contributed about 8800 tons of sulfur to the

33   Antarctic lower stratosphere. This indicates that the long-range transport under favorable

34   meteorological conditions enables tropical volcanic eruptions to be an important remote source of sulfur

35   for the Antarctic stratosphere.

36   **1 Introduction**

37   Over the past two decades, multiple volcanic eruptions injected sulfur into the upper troposphere and

38   lower stratosphere, which has been the dominant source of the stratospheric sulfate aerosol load

39   (Vernier et al., 2011), preventing true background levels from other sources ever being seen (Solomon

40   et al., 2011). Stratospheric sulfate aerosol mainly reflects solar radiation and absorbs infrared radiation,

41   causing cooling of the troposphere and heating of the stratosphere. It contributes to the largest

42   uncertainties to estimates and interpretations of the Earth's changing energy budget (Boucher et al.,

43   2013). Further, by modulating the stratospheric and tropospheric temperature it has an impact on

44   stratospheric dynamics, e. g. it can lead to dramatic phase changes of the quasi-biennial oscillation

45   (Aquila et al., 2014) and alter the spatiotemporal characteristics of the El Niño–Southern Oscillation

46   (ENSO) on both short (few years) and long (decades) timescales (Pausata et al., 2015). Stratospheric

47   sulfate aerosol also has an impact on chemical processes in the lower stratosphere (Jäger and Wege,

48   1990; Solomon et al., 1993), in particular on polar ozone depletion (Tilmes et al., 2008; Drdla and

49   Müller, 2012; Solomon et al., 2016). The presence of H_2SO_4 in the polar stratosphere in combination

50   with cold temperatures facilitates the formation of polar stratospheric clouds (PSCs), which increase

51   heterogeneous ozone depletion chemistry (Solomon et al., 1999; Zuev et al., 2015). Recent healing of

52   Antarctic ozone depletion was constantly disturbed by moderate volcanic eruptions (Solomon et al.,

53   2016). Mid- and high latitude explosive volcanic eruptions may directly influence the polar stratosphere.

54   For example, the aerosol plume from the Calbuco eruption in 2015, including various volcanic gases,

55   penetrated the polar vortex and caused a new record of the size of the Antarctic ozone hole after the

56   eruption (Solomon et al., 2016; Ivy et al., 2017; Stone et al., 2017).

57   Usually, Antarctica is relatively free of local aerosol sources, but aerosols from low latitudes can reach

58   Antarctica through long-range transport (Sand et al., 2017). Some of the sulfate found in the ice cores

59   can be attributed to volcanic eruptions (Mazzera et al., 2001; Gao et al., 2007; Sigl et al., 2015).

60   Measurements of enhanced aerosol in the lower Antarctic stratosphere right above the tropopause were

61   made in October/November 1983, 84 and 85. These enhanced aerosol number concentrations were

62 attributed to aerosol transported to Antarctica from the eruption of the tropical volcano El Chichon in

63 1982 (Hofman and Rosen, 1985; Hofmann et al., 1988). Tropical volcanic eruptions can also enhance

64 polar aerosols by long-range transport. Model results indicate that numerous moderate eruptions have

65 affected ozone distributions over Antarctica, including the Merapi tropical eruption in October 2010

66 (Solomon et al., 2016). However, the transport mechanism is not well represented in present global

67 climate models, and the uncertainties in modeled AOD in both polar regions are large (Sand et al.,

68 2017).

69 The Mount Merapi (7.5°S, 110.4°E, elevation: 2930 m) is an active stratovolcano located in Central

70 Java, Indonesia. Merapi has a long record of eruptive activities. The most recent large eruption with a

71 volcanic explosivity index (VEI) of 4 occurred between 26 October and 7 November 2010 (Pallister et

72 al., 2013), with SO_2 emission rates being a few orders of magnitude higher than previous eruptions.

73 Following the Merapi eruption in 2010, evidence of poleward transport of sulfate aerosol towards

74 southern hemisphere high latitudes was found in time series of aerosol observations by the Michelson

75 Interferometer for Passive Atmospheric Sounding (MIPAS) (Günther et al., 2017) and Cloud-Aerosol

76 Lidar with Orthogonal Polarization (CALIOP) (Khaykin et al., 2017) .

77 There are three main ways for transport out of the tropical tropopause layer (TTL): the deep and shallow

78 branches of the Brewer-Dobson circulation (BDC) and horizontal mixing (Vogel et al., 2011). There is

79 considerable year-to-year seasonal variability in the amount of irreversible transport from the tropics to

80 high latitudes, which is related to both the phase of the QBO and the state of the polar vortex (Olsen et

81 al., 2010). The BDC plays a large role in determining the distributions of many constituents in the

82 extratropical lower stratosphere. And the faster quasi-horizontal transport between the tropics and polar

83 regions also significantly contributes to determining these distributions. The efficiency of transporting

84 constituents quasi-horizontally depends on wave breaking patterns and varies with time of year (Kravitz

85 and Robock, 2011; Wu et al., 2017). Better knowledge of the transport pathways and an accurate

86 representation of volcanic sulfur injections into the upper troposphere and lower stratosphere (UTLS)

87 are key elements for understanding the global stratospheric aerosol budget is key to understanding the

88 cooling effects and ozone loss linked to volcanic activity.

89 The aim of the present study is to investigate the quasi-horizontal transport by tracing the volcanic

90 plume of the Merapi eruption from the tropics to Antarctica and quantifying its contribution to the

91 sulfur load in the Antarctic lower stratosphere. In Sect. 2, the new Atmospheric Infrared Sounder (AIRS)

92 SO_2 observations (Hoffmann et al., 2014), the MIPAS aerosol observations (Griessbach et al., 2016)

93 and the method for reconstructing the SO_2 injection time series of the Merapi eruption are introduced. In

Atmospheric
Chemistry
and Physics
Discussions

94   Sect. 3 the results are presented: first, the reconstructed time series of the Merapi eruption is discussed;

95   second, the dispersion of the Merapi plume is investigated using up to 6 months long Lagrangian

96   forward trajectories initialized with the reconstructed SO_2 time series; third, the simulation is compared

97   to MIPAS volcanic aerosol measurements and the plume dispersion is investigated using MIPAS

98   aerosol detections. In Sect.4 the results are discussed with the background of the meteorological

99   conditions and conclusions are given in Sect. 5.

100   **2 Satellite data, model and method**

101   **2.1 MIPAS instrument and aerosol measurements**

102   MIPAS (Fischer et al., 2008) is an infrared limb emission spectrometer aboard the European Space

103   Agency's (ESA's) Envisat, which provided nearly 10 years of measurements from July 2002 to April

104   2012. MIPAS spectral measurements cover the wavelength range from 4.15 to 14.6 microns. The

105   vertical coverage of MIPAS' nominal measurement mode during the so-called `optimized resolution

106   phase' from January 2005 to April 2012 was 7–72 km. The field of view of MIPAS was about 3 km × 30

107   km (vertically × horizontally) at the tangent point. The extent of the measurement volume along the line

108   of sight was about 300 km, and the horizontal distance between two adjacent limb scans was about 500

109   km. On each day, ~14 orbits with ~90 profiles per orbit were measured. The vertical sampling was 1.5

110   km in the UTLS and 3 km above the UTLS. In 2010 and 2011, MIPAS measured for 4 days in nominal

111   mode followed alternately by one day in middle atmosphere mode or upper atmosphere mode. In this

112   study, we focussed on measurements in the nominal mode.

113   For the aerosol detections, we used the MIPAS altitude-resolved aerosol-cloud-index (ACI) products as

114   introduced by Griessbach et al. (2016) to compare with the MPTRAC simulations and analyze the

115   poleward transport of the Merapi volcanic plume. Small ACI values indicate large aerosol extinction

116   coefficients and vice versa. For instance, MIPAS data points with ACI < 7 can cover infrared extinction

117   coefficients larger than 1×10^{-4} km^{-1}, which corresponds to 3×10^{-4} km^{-1} in the visible wavelength

118   range (Griessbach et al. 2016). Larger ACI values will show aerosol load with even smaller extinction

119   coefficients. As ice clouds usually have extinction coefficients larger than 1×10^{-4} km^{-1}, we applied a

120   brightness-temperature-correlation method, that serves as an ice cloud filter, to all MIPAS spectra with

121   ACI<7 (Griessbach et al., 2016) to remove the ice clouds from the data set. The resulting aerosol

122   product is be sensitive to different types of aerosol, in particular, volcanic ash, sulfate aerosol, mineral

123   dust, as well as non-ice PSCs.

Atmospheric
Chemistry
and Physics
Discussions

2.2 AIRS

AIRS (Aumann et al., 2003) is an infrared nadir sounder with across-track scanning capabilities aboard the National Aeronautics and Space Administration's (NASA's) Aqua satellite. Aqua was launched in 2002 and operates in a nearly polar Sun-synchronous orbit at about 710 km with a period of 98 min. AIRS provides nearly continuous measurement coverage with 14.5 orbits per day and with a swath width of 1780 km it covers the globe almost twice a day. The AIRS footprint size is 13.5 km × 13.5 km at nadir and 41 km × 21.4 km for the outermost scan angles respectively. The along-track distance between two adjacent scans is 18 km. The AIRS observations provide good horizontal resolution and make it ideal for observing the fine filamentary structures of volcanic SO_2 plumes.

In this study, we use an optimized SO_2 index (SI, unit: K) to estimate the amount of SO_2 injected into the atmosphere by the Merapi eruption 2010. The SI is defined as the brightness temperature differences in the 7.3 µm SO_2 waveband.

$$SI = BT \left(1412.87 \text{cm}^{-1} \right) - BT \left(1371.52 \text{ cm}^{-1} \right), \qquad (1)$$

where BT is the brightness temperature measured at wavenumber ν. This SI is more sensitive to low concentrations and performs better on suppressing background interfering signals than the SI provided in the AIRS operational data products. It is an improvement of the SI definition given by Hoffmann et al. (2014) by means of a better choice of the background channel (selecting 1412.87 cm^{-1} rather than 1407.2 cm^{-1}). The SI increases with increasing SO_2 column density and it is most sensitive to SO_2 at altitudes above 3-5 km. SO_2 injections into the lower troposphere are usually not detectable in the infrared spectral region because the atmosphere gets opaque due to the water vapor continuum. A detection threshold of 1 K was used in this study to identify the Merapi SO_2 injections. AIRS detected the Merapi SO_2 cloud from 3 November to 15 November 2010.

2.3 MPTRAC model and reconstruction of the volcanic SO_2 injection time series of the Merapi eruption

In this study, we used the highly scalable MPTRAC model to investigate the volcanic eruption event. In the MPTAC model, air parcel trajectories are calculated based on numerical integration using wind fields from global meteorological reanalyses (Hoffmann et al., 2016; Rößler et al., 2017). Diffusion is modeled by uncorrelated Gaussian random displacements of the air parcels with zero mean and standard deviations $\sigma_x = \sqrt{D_x \Delta t}$ (horizontally) and $\sigma_z = \sqrt{D_z \Delta t}$ (vertically). D_x and D_z are the horizontal and vertical diffusivities respectively, and Δt is the time step for the trajectory calculations. For the

Atmospheric
Chemistry
and Physics
Discussions

154   Merapi simulation, D_x and D_z were set to 50 m^2 s^{-1} and 0 m^2 s^{-1} in the troposphere and 0 m^2 s^{-1} and 0.1

155   m^2 s^{-1} in the stratosphere, respectively. In addition, sub-grid scale wind fluctuations, which are

156   particularly important for long-range simulations, are simulated by a Markov model (Stohl et al., 2005;

157   Hoffmann et al., 2016). Loss processes of chemical species, SO$_2$ in our case, are simulated based on an

158   exponential decay of the mass assigned to each air parcel. In the stratosphere a constant half lifetime of

159   7 days was assumed for SO$_2$. Considering that the Merapi eruption occurred in the humid tropics, with

160   high concentration of hydroxyl radical, a half lifetime of 2.5 days was assumed for the troposphere.

161   To estimate the time- and altitude-resolved SO$_2$ injections, we follow the approach of Hoffmann et al.

162   (2016) and Wu et al. (2017) and use backward trajectories calculated with the MPTRAC model together

163   with AIRS SO$_2$ measurements. Observations from 3 to 7 November 2010 were used for estimating the

164   SO$_2$ injection during the explosive eruption. Since the AIRS measurements do not provide altitude

165   information, we established a column of air parcels at each AIRS SO$_2$ detection. The vertical range of

166   the column was set to 0–25 km, covering the possible vertical dispersion range of the SO$_2$ plume in the

167   first few days. The AIRS footprint size varies between 14 and 41 km, hence in the horizontal direction,

168   we chose an average of 30 km as the full width at half maximum (FWHM) for the Gaussian scatter of

169   the air parcels. In our simulation, a fixed total number of 100,000 air parcels was assigned to all air

170   columns and the number of air parcels in each column was scaled linearly proportional to the SO$_2$ index.

171   Then backward trajectories were calculated for all air parcels, and trajectories that were at least 2 days

172   but no more than 5 days long and that passed the volcano domain were recorded as emissions of Merapi.

173   The volcano domain was defined by means of a search radius of 75 km around the location of the

174   Merapi and 0–20 km in the vertical direction, covering all possible injection heights. Sensitivity

175   experiments have been conducted to optimize these pre-assigned parameters to obtain the best

176   simulation results. Our estimates of the Merapi SO$_2$ injection are shown in Sect. 3.

177   Starting with the reconstructed altitude-resolved SO$_2$ injection time series, the transport of the Merapi

178   plume is simulated for 6 months, covering the time period from the initial eruption on 26 October 2010

179   to 30 April 2011. The trajectory calculations are driven by the ERA–Interim data (Dee et al., 2011)

180   interpolated on a 1°× 1° horizontal grid on 60 model levels with the vertical range extending from the

181   surface to 0.1 hPa. The ERA–Interim data are provided at 00, 06, 12 and 18 UTC. Outputs of model

182   simulations are given every 3 hours at 00, 03, 06, 09, 12, 15, 18 and 21 UTC. The impact of different

183   meteorological analysis on MPTRAC simulations was assessed by Hoffmann et al. (2016, 2017). In

184   both studies the ERA–Interim data showed good performance.

3 Results

Figure 1 displays the time-latitude section of MIPAS aerosol detections with median ACI value in each bin smaller than 7 and within the vertical range of 13 and 20 km, covering the tropical tropopause layer (TTL) and the extratropical lowermost stratosphere (LMS). The MIPAS data captured all the major events that contributed to the aerosol load in the UTLS, i.e., moderate volcanic eruptions from 2002 to 2012 and one large bushfire in 2009, as well as the subsequent dispersion and change of aerosol load over time. Particularly, after the Merapi eruption in 2010, marked by the red triangle in Fig. 1, the MIPAS data show an obvious poleward transport of aerosol from the tropics to Antarctica.

3.1 Merapi eruption and SO_2 injection time series

According to the chronology of the Merapi eruption (Surono et al., 2012), the explosive eruption first occurred between 10:00 and 12:00 UTC on 26 October and this eruption generated a plume that reached 12 km altitude. A period of relative small explosive eruptions continued from 26 October to 31 October. During the initial period of the dome growth (1–3 November), the level of SO_2 degassing was relatively low compared with the SO_2 degassing before 1 November. On 3 November, the eruptive intensity increased again accompanied by much stronger degassing and a series of explosions. The intermittent explosive eruptions occurred during 4–5 November with the climactic eruption on 4 November, producing an ash column that reached up to 17 km altitude. From 6 November, explosive activity decreased slowly and the degassing declined.

Figure 2 shows the time- and altitude-resolved SO_2 injections of the Merapi eruption retrieved using the AIRS SO_2 index data and the backward-trajectory approach. It successfully reproduced the chronology of the Merapi eruption as outlined by Surono et al. (2012). Significant SO_2 was injected into altitudes below 8 km during the initial explosive eruptions on 26–30 October. Starting from 30 October the plume reached up to 12 km. During 1–3 November the SO_2 injections into altitudes below 12 km continued but the mass was less than in the initial phase. On 3 November the intensity increased again and peaked in the climactic explosive eruptions of 4–5 November. Before 3 November the reconstruction indicates a minor fraction of SO_2 right above the tropopause.

To study the long-range transport of the Merapi plume, we initialized 100,000 air parcels at the SO_2 injection time series shown in Fig. 2 with a SO_2 mass of 0.44 Tg as provided in Surono et al. (2012) and calculated forward trajectories for 6 months. Here, we only considered the plume in the upper troposphere and stratosphere where the lifetime of both SO_2 and sulfate aerosol is longer than that in the lower troposphere. Further, the SO_2 was all converted into sulfate aerosol within a few weeks (von

Atmospheric
Chemistry
and Physics
Discussions

216   Glasow et al., 2009; we could also see it in the AIRS SO_2 and MIPAS aerosol data), and we assumed

217   that the sulfate aerosol converted from SO_2 remains collocated with the SO_2 plume, i.e., the

218   sedimentation of small sulfate aerosol particles was negligible for the timescale considered.

219   Figure 3 shows the evolution of the simulated Merapi plume and compares the plume altitudes to the

220   aerosol top altitudes measured by MIPAS between 7 and 23 November. Immediately after the eruption,

221   the majority of the plume moved towards the southwest and was entrained by the anticyclonic

222   circulation of the tropical cyclone Anggrek (not shown). After the Anggrek weakened and dissipated,

223   the majority of the plume parcels in upper troposphere moved eastward and those in the lower

224   stratosphere moved westward.   In general, the altitudes of the simulated plume are comparable to the

225   MIPAS observations. The remaining discrepancies of air parcel altitudes being higher than the altitudes

226   of MIPAS aerosol detections can be attributed to the fact that the MIPAS tends to underestimate aerosol

227   top cloud altitudes, which is about 0.9 km in case of low extinction aerosol layers and can reach down

228   to -4.5 km in case of broken cloud conditions (Höpfner et al., 2009).

3.2 Meteorological background conditions after the Merapi eruption

230   The Merapi eruption in October 2010 occurred during the seasonal transition from austral spring to

231   summer when the polar vortex typically weakens and the ozone hole shrinks. As depicted in Fig. 4, the

232   meteorological conditions at the polar lower stratosphere (150hPa, ~12km) after the eruption deviated

233   from the climatological mean. The minimum temperature south of 50°S (Fig. 4a) was much lower than

234   the climatological mean during mid-November to mid-December but still higher than the low

235   temperature necessary for existence of PSCs. The polar mean temperature in Fig. 4b, defined as the

236   temperature averaged over latitudes south of 60°S, stayed lower than the climatological mean from

237   November 2010 until February 2011. Corresponding to the low temperatures, the average zonal wind

238   speed at 60°S (Fig. 4c) was significantly larger than the climatological mean value from November

239   2010 to mid-January 2011. The eddy heat flux in Fig. 4d is the product of meridional wind departures

240   and temperature departures from the respective zonal mean values. A more negative value of eddy heat

241   flux indicates that wave systems are propagating into the stratosphere and are warming the polar region.

242   There is a strong anticorrelation between temperature and the 45-day average of the eddy heat flux

243   lagged prior to the temperature. Comparing with the climatological mean state, the polar vortex was

244   more disturbed during mid-July to end of August. But from mid-October to late November, the heat

245   flux was much smaller than the long-term average, which meant a reduction in dynamical disturbances

246   of the polar vortex as the QBO changed into a strong westerly phase. Considering the temperature, the

247   subpolar wind speed and the heat flux, the polar vortex was colder and stronger in November and

248   December 2010 compared with the same time in other years. The study of Klekociuk et al. (2011) also

249   confirmed that the polar vortex area was consistently larger than the climatological mean particularly

250   during November and December (see their Fig. 9). Consistent with the strength of the polar vortex, in

251   November and December 2010 the ozone hole area in Fig. 4e, defined as the region of ozone values

252   below 220 Dobson Units (DU) located south of 40°S, was larger than the climatological mean.

253   Meanwhile, the low polar mean temperature and stable polar vortex resulted in a long-lasting ozone

254   hole, which disappeared in the last week of December. The polar vortex broke down by mid-January

255   2011 when subpolar wind speed decreased below 15 m/s (Fig. 4c).

256   The poleward transport from the tropics to the polar region is known to be modulated by the phase of

257   the quasi-biennial oscillation (QBO) and the state of the polar vortex itself: Fig. 4f shows that just before

258   the Merapi eruption in 2010, the QBO switched from easterly phase to westerly phase. The westerly

259   phase of the QBO promotes meridional transport from the tropics to subtropics, especially into the

260   winter hemisphere (O'Sullivan and Dunkerton, 1997; Shuckburgh et al., 2001; Jäger, 2005). However, it

261   also results in zonal wind acceleration at the high latitudes (Watson and Gray, 2014; Holton and Tan,

262   1980) and a less dynamically disturbed polar vortex (Anstey and Shepherd, 2014; Baldwin and

263   Dunkerton, 1999), which will make it less possible for air parcels to penetrate the polar vortex.

264   **3.3 Lagrangian simulation and satellite observation of poleward transport of the Merapi plume**

265   The early plume evolution until about one month after the initial eruption is shown on the maps in Fig.

266   3 together with MIPAS observations of volcanic aerosol (only aerosol detections with ACI<7 are

267   shown). Within about one month after the initial eruption, the plume was nearly entirely transported

268   around the globe in the tropics, moving west at altitudes of about 17 km. The lower part of the plume,

269   below about 17 km was transported south-eastward and reached latitudes south of 30°S by

270   mid-November. The simulated long-term transport of the Merapi plume is illustrated in Fig. 5, showing

271   the relative number of air parcels reaching a latitude-altitude bin every half a month. To verify the

272   model results, the poleward transport of aerosols as detected by MIPAS is shown in Fig. 6. For

273   comparison, only simulation results above the minimum altitude of MIPAS aerosol detections in Fig. 6

274   are shown in Fig. 5. In this study, we only focus on aerosol distributions in the upper troposphere and

275   stratosphere, where sulfate aerosol has a longer lifetime and potential climate impacts.

276   During the first month after the eruption (Figs. 5a–b), the majority of the plume was transported

277   southward roughly along the isentropic surfaces. The most significant pathway is above the core of the

Atmospheric
Chemistry
and Physics
Discussions

Open Access

EGU

278 subtropical jet in the southern hemisphere. However, because of the transport barrier of the polar jet

279 during austral spring, the plume was confined to the north of 60°S. In December 2010 (Figs. 5c–d), a

280 larger fraction of the plume was transported southward above the subtropical jet core, and deep into the

281 polar region south of 60°S as the polar jet broke up. Till the end of January 2011, the majority of the

282 plume had entered the mid- and high latitudes in the southern hemisphere, whereas only a very small

283 proportion of the plume was transported north of 30°N. Substantial quasi-horizontal poleward transport

284 from the TTL towards the LMS in Antarctica was found from November 2010 to February 2011 (Figs.

285 5a–h), approximately between 350 and 480 K (~10–20 km). From March to April 2011(Figs. 5i–l), the

286 proportion of the plume that went across 60°S stopped increasing and the maxima of the plume

287 descended from 380 to 350 K. During this transport towards Antarctica, a secondary upward transport

288 split from the plume, which was particularly observable from January 2011 till the end of the simulation

289 in April 2011(Figs. 5e–l). This slow upward transport was mainly located around 15°S above the

290 tropopause and can be attributed to the upward branch of the BDC.

291 The poleward transport in the MPTRAC simulations was confirmed by MIPAS aerosol detections.

292 MIPAS ACI zonal median values are shown in Fig. 6 for all MIPAS measurements after filtering out

293 ice clouds. Small ACI values indicate a large aerosol load and large ACI values indicate clear air. As

294 seen in Fig. 6, the locally confined aerosol plume from the Merapi eruption did not dominate the zonal

295 median during the first half month after the eruption (Fig. 6a), but became evident between 350 and 380

296 K around the latitude of 7.5°S by the end of November (Fig. 6b) as the plume was transported around

297 the globe in the tropics. As shown in the MPTRAC simulations, the transport towards the northern mid-

298 and high latitudes was suppressed by the strong subtropical jets. The transport of the volcanic plume

299 towards Antarctica in the UTLS region was observed from December 2010 to February 2011 (Figs. 6c–

300 h) consistent with the simulations. The MIPAS aerosol data also demonstrated the upward transport

301 from the tropical upper troposphere to the stratosphere, which was observed after late January 2010.

302 The aerosol transported upward had increased the aerosol load in the tropical stratosphere reservoir

303 compared to the aerosol load before the Merapi eruption.

304 Fig. 6 verified aerosol transport from the tropics to Antarctica and upward into the tropical stratosphere.

305 However, before the eruption of Merapi, the aerosol load in the tropical stratosphere was already

306 elevated by several small and moderate-size volcanic eruptions, namely the Sarychev Peak (12 Jun

307 2009), Nyamuragira (20 Jan 2010), Soufriere Hills (11 Feb 2010) and Pacaya (28 May 2010). In order

308 to infer the increase of the aerosol load due to the eruption of Merapi from the MIPAS data, we

309 calculated the median ACI between 1–4 November 2010 when there was no aerosol from the Merapi

Atmospheric
Chemistry
and Physics
Discussions

310   eruption, to define the "background" aerosol load and then remove this "background" from the median

311   ACI in Fig. 6. The results shown in Fig.7 demonstrate the change of median ACIs in the tropics and

312   southern hemisphere corresponding to the same time period as Fig. 6, with positive/negative values

313   indicating an increase/decrease of aerosol load. No significant change was observed during the first half

314   month after the eruption due to the zonal averaging degrading the aerosol signal (Fig. 7a). The largest

315   increase first appeared in the upper troposphere directly above Mount Merapi (Fig. 7b) and then moved

316   quasi-horizontally southward into the UTLS region to ~40°S (Figs. 7c–f), consistent with what Figs. 5

317   and 6 showed. A relatively small but still significant increase of aerosol south of 60°S in the tropopause

318   region was found from January 2011 (Fig. 7e) and it lasted until mid- April 2011 (Fig. 7j). Six months

319   after the eruption, the aerosol levels were still slightly elevated in the tropical upper troposphere above

320   350 K. There should have been a decrease of the aerosol load in the tropical stratosphere because of

321   sedimentation and poleward transport of aerosol if there were no aerosol from the Merapi eruption. But

322   the upward transport of the Merapi aerosol compensated the loss.

323   **3.4 Efficiency of quasi-horizontal transport from the tropics to Antarctica**

324   As the results of the Lagrangian transport simulations with the MPTRAC model were comparable to the

325   MIPAS observations (Sect. 3.3), it was possible not only to demonstrate the transport pathways but also

326   to estimate the efficiency of the transport. The MPTRAC simulations and the MIPAS observations have

327   demonstrated transport on the "surf zone" that reaches from the subtropics to high latitudes (Holton et

328   al., 1995), where air masses are affected by both fast meridional transport and the slow BDC. Our data

329   show that quasi-horizontal mixing in the lower extratropical stratosphere between 350 and 480 K is the

330   main transport pathway for the volcanic aerosol. Figure 8 illustrates how the volcanic plume between

331   350 and 480 K approached Antarctica over time. Gray dashed and solid lines mark potential vortices

332   (PV) contours with the largest PV gradients on the 350 and 480 K isentropic surfaces. These

333   dynamically relevant PV contours represent horizontal transport barriers for air masses on the respective

334   isentropic surface. On isentropic surfaces below 380 K, the contours of maximum PV gradients

335   represent the dynamical discontinuity near the core of the subtropical jet stream and thus represent a

336   transport barrier between the tropics and midlatitudes (Haynes and Shuckburgh, 2000; Kunz et al.,

337   2011a,b). Isentropic transport of air masses across these boundaries indicates exchange between the

338   tropics and extratropics due to Rossby wave breaking. On isentropic surfaces above 400 K, the contours

339   of maximum PV gradients represent a boundary in the lower stratosphere, in particular, due to the polar

340   vortices in winter (Kunz et al., 2015). For comparison we have also shown contour lines of ozone

Atmospheric
Chemistry
and Physics
Discussions

341 column density of 220 DU (black isolines in Fig. 8), indicating the location and size of the ozone hole.

342 The PV boundary on 480 K is in most cases collocated with the area of the ozone hole, showing that

343 both quantities provide a consistent representation of the area of the polar vortex.

344 The Merapi volcanic plume first reached the 350 K transport boundary in mid-November and went

345 close to the 480 K transport boundary in December. The long-lasting polar vortex prevented the

346 volcanic plume from crossing the transport boundary in the beginning of December, but from

347 mid-December, the polar vortex became more disturbed and displaced from the south pole, together

348 with a shrinking ozone hole. As mentioned in Sect.3.2, the ozone hole broke up at the end of December

349 2010 and the polar vortex broke down by mid-January 2011.

350 The fractions of the volcanic plume that crossed the individual transport boundaries or the latitude of

351 60°S on each isentropic surface are shown in Fig. 9. In both cases, the proportion increased from

352 November 2010 to January 2011. In November and December 2010 the largest plume transport across

353 the transport boundaries occurred between the 360 and 430 K isentropic surface (Fig. 9a), with a peak at

354 380–390 K. In January and February 2011 the peak was slightly elevated to 390–400 K. In November

355 2010, the volcanic plume did not cross the 480 K transport boundary of the polar vortex at high altitudes,

356 especially above about 450 K. The high-latitude fraction kept increasing from December 2010 to

357 February 2011 as the weakening of the polar vortex made the transport boundary more permeable. In

358 March and April 2011, the total proportion decreased and the peak descended to 370 K in March and

359 further to 360 K in April. The proportion of the volcanic plume south of 60°S (Fig. 9b) increased

360 slightly from November to December 2010, and then increased significantly from December 2010 to

361 January and February 2011 at all altitudes as the polar vortex displaced and broke down. Finally, the

362 transport to south of 60°S started to decrease in March 2011. From November 2010 to February 2011

363 the peak was around 370–400 K, but in March and April 2011 the peak resided around 350–370 K.

364 Figure 10 summarizes the poleward transport of the volcanic plume between 350 and 480 K. The

365 zonally resolved fractions derived from the Lagrangian MPTRAC simulations and the fraction of air

366 parcels south of 60°S are shown in Fig. 10a. Figure 10b demonstrates the increasing and decreasing

367 aerosol load in this vertical range for MIPAS aerosol detections relative to 1–4 November median (see

368 Sect.3.3). The poleward transport trend in Fig. 10a is comparable to the poleward migration of the

369 enhanced aerosol in Fig. 10b. The simulations show that the plume reached 60°S by the end of

370 November 2010. Correspondingly, the aerosol load south of 60°S was elevated when the volcanic

371 plume was transported there. The percentage fluctuated, but increased until the end of February 2011,

372 with a maximum percentage of about 4%. A steep increase occurred from mid-December 2010 to end of

Atmospheric
Chemistry
and Physics
Discussions

373 January 2011, following the displacement and breakdown of the polar vortex. The elevated aerosol load

374 south of 60°S decreased from March 2011, because the plume descended to altitudes below 350 K as

375 shown by Fig. 9b. Overall, enhanced aerosol due to Merapi eruption was observed mostly in the

376 subtropics and midlatitudes, but the aerosol load in the south polar region was also significantly

377 elevated for three months from December 2010 to February 2011.

378 **4 Discussion**

379 The results presented in Sect. 3 show that the meridional transport of the Merapi volcanic plume to

380 Antarctica mostly occurred between the isentropic surfaces of 350 and 480 K (about 10 to 20 km),

381 covering the TTL and the lower stratosphere at mid- and high latitudes. For this long-range transport on

382 timescales of a few months, fast isentropic transport associated with quasi-horizontal mixing was found

383 to be the most efficient pathway. The phase of QBO, subtropical Rossby wave breaking and the strength

384 and stability of the polar vortex all have an impact on the transport efficiency. The Merapi eruption

385 occurred in austral spring and fast poleward transport was facilitated by the weakening subtropical jet

386 and active Rossby wave breaking events. The westerly QBO enhanced transport and mixing in the

387 subtropics with implications on the position of the subtropical barrier (Shuckburgh et al., 2001; Palazzi et

388 al., 2011). The QBO also modulated the ability of upward propagating planetary waves to influence the

389 strength of the polar vortex. Although the polar vortex was relatively stable when the Merapi eruption

390 occurred, after the volcanic plume reached the south polar region, the polar vortex was displaced from

391 the south pole and distorted because more wave systems propagated into the polar stratosphere and

392 warmed the polar region, so that the volcanic plume could be transported from the tropics deep into

393 Antarctica under all these favourable conditions.

394 The phase of the QBO influences the amount of volcanic emissions transported out of tropics, while the

395 heating effect of a large amount of sulfur injected by volcanic eruptions can change the pattern of the

396 QBO (Niemeier and Schmidt, 2017). With increasing emission rates the velocity of the equatorial jet

397 streams increases and less sulfate is transported out of the tropics. The amount of SO_2 injected during

398 the Merapi eruption 2010 was 0.44 Tg, far less than the 8 TgS/yr required to shut down or reverse the

399 QBO pattern (Niemeier and Schmidt, 2017), so that the westerly phase of the QBO that promote

400 meridional transport was under minor influence of the heating effect of sulfur in this case.

401 Based on the simulations in Sect. 3.4, up to ~4% of air parcels composed of SO_2 and sulfate aerosol

402 were transported from the TTL to the lower stratosphere in the south polar region till the end of

Atmospheric
Chemistry
and Physics
Discussions

403 February 2011, which means the Merapi eruption contributed about 8800 tons of sulfur to the polar

404 lower stratosphere within 4 months after the eruption, assuming that the sulfate aerosol converted from

405 SO_2 remained in the plume. In the lower stratosphere, the atmosphere is relatively dry and clean

406 compared with the lower troposphere, so the sulfate aerosols may have a smaller chance to interact with

407 clouds or to be washed out. In fact, in the polar lower stratosphere usually sedimentation and downward

408 transport by the BDC are the main removal processes. Clouds and washout processes usually cannot be

409 expected in the lower stratosphere. However, the amount of sulfate aerosols in the plume could also be

410 affected by other mechanisms that speed up the loss of sulfur, for example, coagulation in the volcanic

411 plume, the absorption of sulfur onto fine ash particles etc. But for a moderate eruption, such as the

412 Merapi eruption, sulphuric particle growth may not be as significant as it is in a large volcanic eruption,

413 so the scavenging efficiency of sulfur will be low.

414 Besides, a kinematic trajectory model like MPTRAC, in which reanalysis vertical wind is used as

415 vertical velocity, typically shows higher vertical dispersion in the equatorial lower stratosphere

416 compared with a diabatic trajectory model (Schoeberl et al., 2003; Wohltmann and Rex, 2008; Liu et al.,

417 2010; Ploeger et al., 2010, 2011). However, the ERA–Interim reanalysis data used in this study to drive

418 the model may constrain the vertical dispersion much better than older reanalyses (Liu et al., 2010;

419 Hoffmann et al., 2017). The meridional transport in this study was mainly quasi-horizontal transport in

420 the mid- and high latitude UTLS region, so the effect of the vertical speed scheme is limited.

421 Meanwhile, the MIPAS aerosol detections confirmed the MPTRAC simulations, so our results can be

422 considered as a representative value.

423 The aerosol transported to the polar lower stratosphere will finally descend with the downward flow in

424 the polar region to lower altitudes, and have a chance to become a nonlocal source of sulfur for

425 Antarctica by dry and wet deposition, following the general precipitation patterns. Quantifying the

426 sulfur deposition flux onto Antarctica is beyond the scope of this study, though. Model results of

427 Solomon et al. (2016) suggest that the Merapi eruption made a small but significant contribution to

428 ozone depletion over Antarctica in the vertical range of 200–100 hPa (~10–14 km). This altitude range

429 is in agreement with our results, where we found transport into the Antarctic stratosphere between 10

430 and 20 km. When the volcanic plume was transported to Antarctica in December 2010, the polar

431 synoptic temperature at these low height levels was already too high for the formation of PSCs. The

432 additional ozone depletion found by Solomon et al. (2016) together with the fact that sulfate aerosol was

433 transported from the Merapi into the Antarctic stratosphere between November and February where no

434 PSCs are present during polar summer, may support the study which suggested that significant ozone

Atmospheric
Chemistry
and Physics
Discussions

435 depletion can also occur on cold binary aerosol (Drdla and Müller, 2012). The Merapi eruption in 2010

436 could be an interesting case study for more sophisticated geophysical models to study the aftermath of

437 volcanic eruptions on polar processes.

5 Summary and conclusion

439 In this study, we analyzed the poleward transport pathway and the transport efficiency of volcanic

440 aerosol released by the Merapi eruption in October 2010 from tropics to the Antarctic lower

441 stratosphere. The analysis was based on AIRS SO_2 measurements, MIPAS sulfate aerosol detections

442 and MPTRAC transport simulations. First, we estimated altitude-resolved SO_2 injection time series

443 during the explosive eruption period using AIRS data together with a backward trajectory approach.

444 Second, the long-range transport of the volcanic plume from the initial eruption to 30 April 2010 was

445 simulated based on the derived SO_2 injection time series. Then the evolution and the poleward

446 migration of the volcanic plume was analyzed and validated with MIPAS aerosol measurements.

447 Results of this study suggest that the volcanic plume from the Merapi eruption was transported from the

448 tropics to south of 60°S within a time scale of one month. Later on a significant fraction of the volcanic

449 plume crossed 60°S, even further to Antarctica until the end of February 2011. As a result, the aerosol

450 load in the Antarctic lower stratosphere was significantly elevated for 3 months from December 2010 to

451 February 2011. From March 2011, the aerosol transported to the polar lower stratosphere descended

452 with the downward flow of the Brewer-Dobson circulation to lower altitudes. This relatively fast

453 meridional transport and the distribution of volcanic aerosol was mainly carried out by quasi-horizontal

454 mixing from the TTL to the extratropical lower stratosphere, which in turn was facilitated by the

455 weakening of the subtropical jet in the seasonal transition from austral spring to summer. Based on the

456 simulations, the most efficient pathway for this quasi-horizontal mixing occurred between isentropic

457 surfaces of 360 to 430 K. The polar vortex in late austral spring 2010 was relatively strong compared to

458 the climatological mean state. However, when the plume went to the south polar region, the polar vortex

459 was displaced off the south pole, so that the volcanic plume was able to enter to the south pole without

460 even penetrating the polar vortex.

461 Overall, after the Merapi eruption, the largest increase of aerosol load occurred in the southern

462 hemisphere midlatitudes and a relatively small but significant fraction of the volcanic plume (4%) was

463 further transported to the Antarctic lower stratosphere within 4 months after the eruption. This

464 contributed 8800 tons of sulfur to the Antarctic stratosphere, which indicates that long-range transport

Atmospheric
Chemistry
and Physics
Discussions

465   under favorable meteorological conditions enables tropical volcanic eruptions to be an important remote

466   source of sulfur to Antarctica.

467   *Code and data availability.* AIRS data are distributed by the NASA Goddard Earth Sciences Data

468   Information and Services Center. The SO_2 index data used in this study (Hoffmann et al., 2014) are

469   available for download at https://datapub.fz-juelich.de/slcs/airs/volcanoes/ (last access: 17 December

470   2017). Envisat MIPAS Level-1B data are distributed by the European Space Agency. The ERA–Interim

471   reanalysis data (Dee et al., 2011) were obtained from the European Centre for Medium-Range Weather

472   Forecasts. The code of the Massive-Parallel Trajectory Calculations (MPTRAC) model is available

473   under the terms and conditions of the GNU General Public License, Version 3 from the repository at

474   https://github.com/slcs-jsc/mptrac (last access: 31 December 2017).

475

476   *Competing interests.* The authors declare that they have no conflict of interest.

477

481   **Reference**

482   Anstey, J. A., and Shepherd, T. G.: High-latitude influence of the quasi-biennial oscillation, Q. J. R.
483   Meteorol. Soc., 140, 1-21, doi: 10.1002/qj.2132, 2014.
484   Aquila, V., C. I. Garfinkel, P.A.Newman, L. D. Oman, and D. W. Waugh, Modifications of the
485   quasi-biennial oscillation by a geoengineering perturbation of the stratospheric aerosol layer,
486   Geophys. Res. Lett., 41, 1738-1744, doi: 10.1002/2013GL058818, 2014.
487   Aumann, H. H., Chahine, M. T., Gautier, C., Goldberg, M. D., Kalnay, E., McMillin, L. M., Revercomb,
488   H., Rosenkranz, P. W., Smith, W. L., Staelin, D. H., Strow, L. L., and Susskind, J.: AIRS/AMSU/HSB
489   on the Aqua mission: design, science objectives, data products, and processing systems, IEEE Trans.
490   Geosci. Remote Sens., 41, 253-264, doi: 10.1109/TGRS.2002.808356, 2003.
491   Baldwin, M. P., and Dunkerton, T. J.: Propagation of the Arctic Oscillation from the stratosphere to the
492   troposphere, J. Geophys. Res. Atmos., 104, 30937-30946, doi: 10.1029/1999JD900445, 1999.
493   Dee, D. P., Uppala, S. M., Simmons, A. J., Berrisford, P., Poli, P., Kobayashi, S., Andrae, U.,
494   Balmaseda, M. A., Balsamo, G., Bauer, P., Bechtold, P., Beljaars, A. C. M., van de Berg, L., Bidlot,
495   J., Bormann, N., Delsol, C., Dragani, R., Fuentes, M., Geer, A. J., Haimberger, L., Healy, S. B.,
496   Hersbach, H., Holm, E. V., Isaksen, L., Kallberg, P., Kohler, M., Matricardi, M., McNally, A. P.,
497   Monge-Sanz, B. M., Morcrette, J. J., Park, B. K., Peubey, C., de Rosnay, P., Tavolato, C., Thepaut, J.
498   N., and Vitart, F.: The ERA-Interim reanalysis: configuration and performance of the data
499   assimilation system, Q. J. R. Meteorol. Soc., 137, 553-597, doi: 10.1002/qj.828, 2011.
500   Drdla, K., and Müller, R.: Temperature thresholds for chlorine activation and ozone loss in the polar
501   stratosphere, Ann. Geophys., 30, 1055-1073, doi: 10.5194/angeo-30-1055-2012, 2012.

Atmospheric
Chemistry
and Physics
Discussions

502 Fischer, H., Birk, M., Blom, C., Carli, B., Carlotti, M., von Clarmann, T., Delbouille, L., Dudhia, A.,
503   Ehhalt, D., Endemann, M., Flaud, J. M., Gessner, R., Kleinert, A., Koopman, R., Langen, J.,
504   López-Puertas, M., Mosner, P., Nett, H., Oelhaf, H., Perron, G., Remedios, J., Ridolfi, M., Stiller, G.,
505   and Zander, R.: MIPAS: an instrument for atmospheric and climate research, Atmos. Chem. Phys., 8,
506   2151-2188, doi: 10.5194/acp-8-2151-2008, 2008.
507 Gao, C., Oman, L., Robock, A., and Stenchikov, G. L.: Atmospheric volcanic loading derived from
508   bipolar ice cores: Accounting for the spatial distribution of volcanic deposition, J. Geophys. Res.
509   Atmos., 112, D09109, doi: 10.1029/2006JD007461, 2007.
510 Griessbach, S., Hoffmann, L., Spang, R., von Hobe, M., Müller, R., and Riese, M.: Infrared limb emission
511   measurements of aerosol in the troposphere and stratosphere, Atmos. Meas. Tech., 9, 4399-4423,
512   doi:10.5194/amt-9-4399-2016, 2016.
513 Günther, A., Höpfner, M., Sinnhuber, B. M., Griessbach, S., Deshler, T., von Clarmann, T., and Stiller,
514   G.: MIPAS observations of volcanic sulphate aerosol and sulphur dioxide in the stratosphere, Atmos.
515   Chem. Phys. Discuss., 2017, 1-32, doi: 10.5194/acp-2017-538, 2017.
516 Haynes, P., and Shuckburgh, E.: Effective diffusivity as a diagnostic of atmospheric transport: 2.
517   Troposphere and lower stratosphere, J. Geophys. Res. Atmos., 105, 22795-22810, doi:
518   10.1029/2000JD900092, 2000.
519 Heng, Y., Hoffmann, L., Griessbach, S., Rößler, T., and Stein, O.: Inverse transport modeling of volcanic
520   sulfur dioxide emissions using large-scale simulations, Geosci. Model Dev., 9, 1627-1645,
521   doi:10.5194/gmd-9-1627-2016, 2016.
522 Hoffmann, L., Griessbach, S., and Meyer, C. I.: Volcanic emissions from AIRS observations: detection
523   methods, case study, and statistical analysis, in: Remote Sensing of Clouds and the Atmosphere XIX
524   and Optics in Atmospheric Propagation and Adaptive Systems XVII, edited by: Comeron, A.,
525   Kassianov, E. I., Schafer, K., Picard, R. H., Stein, K., and Gonglewski, J. D., Proceedings of SPIE,
526   Spie-Int Soc Optical Engineering, Bellingham, doi: 92421410.1117/12.2066326, 2014.
527 Hoffmann, L., Hertzog, A., Rößler, T., Stein, O., and Wu, X.: Intercomparison of meteorological
528   analyses and trajectories in the Antarctic lower stratosphere with Concordiasi superpressure balloon
529   observations, Atmos. Chem. Phys., 17, 8045-8061, doi: 10.5194/acp-17-8045-2017, 2017.
530 Hoffmann, L., Rößler, T., Griessbach, S., Heng, Y., and Stein, O.: Lagrangian transport simulations of
531   volcanic sulfur dioxide emissions: Impact of meteorological data products, J. Geophys. Res. Atmos.,
532   121, 4651-4673, doi: 10.1002/2015JD023749, 2016.
533 Hofmann, D. J., Rosen, J. M., and Gringel, W.: Delayed production of sulfuric acid condensation nuclei
534   in the polar stratosphere from El Chichon volcanic vapors, Journal of Geophysical Research:
535   Atmospheres, 90, 2341-2354, doi:10.1029/JD090iD01p02341, 1985.
536 Hofmann, D. J., Rosen, J. M., and Harder, J. W.: Aerosol measurements in the winter/spring Antarctic
537   stratosphere: 1. Correlative measurements with ozone, Journal of Geophysical Research:
538   Atmospheres, 93, 665-676, doi:10.1029/JD093iD01p00665, 1988.
539 Holton, J. R., Haynes, P. H., McIntyre, M. E., Douglass, A. R., Rood, R. B., and Pfister, L.:
540   Stratosphere-troposphere exchange, Reviews of Geophysics, 33, 403-439, doi: 10.1029/95RG02097,
541   1995.
542 Holton, J. R., and Tan, H. C.: The Influence of the Equatorial Quasi-Biennial Oscillation on the Global
543   Circulation   at   50   mb,   J.   Atmos.   Sci.,   37,   2200-2208,   doi:
544   10.1175/1520-0469(1980)037<2200:tioteq>2.0.co;2, 1980.
545 Höpfner, M., Pitts, M. C., and Poole, L. R.: Comparison between CALIPSO and MIPAS observations
546   of polar stratospheric clouds, Journal of Geophysical Research: Atmospheres, 114,
547   doi:10.1029/2009JD012114, 2009.

Atmospheric
Chemistry
and Physics
Discussions

548   Ivy, D. J., Solomon, S., Kinnison, D., Mills, M. J., Schmidt, A., and Neely, R. R.: The influence of the
549   Calbuco eruption on the 2015 Antarctic ozone hole in a fully coupled chemistry-climate model,
550   Geophys. Res. Lett., 44, 2556-2561, doi: 10.1002/2016GL071925, 2017.

551   Jäger, H.: Long-term record of lidar observations of the stratospheric aerosol layer at
552   Garmisch-Partenkirchen, J. Geophys. Res. Atmos., 110, D08106, doi: 10.1029/2004JD005506, 2005.

553   Jäger, H., and Wege, K.: Stratospheric ozone depletion at northern midlatitudes after major volcanic
554   eruptions, J. Atmos. Chem., 10, 273-287, doi: 10.1007/bf00053863, 1990.

555   Khaykin, S. M., Godin-Beekmann, S., Keckhut, P., Hauchecorne, A., Jumelet, J., Vernier, J. P.,
556   Bourassa, A., Degenstein, D. A., Rieger, L. A., Bingen, C., Vanhellemont, F., Robert, C., DeLand,
557   M., and Bhartia, P. K.: Variability and evolution of the midlatitude stratospheric aerosol budget from
558   22 years of ground-based lidar and satellite observations, Atmos. Chem. Phys., 17, 1829-1845, doi:
559   10.5194/acp-17-1829-2017, 2017.

560   Klekociuk, A., Tully, M., Alexander, S., Dargaville, R., Deschamps, L., Fraser, P., Gies, H., Henderson,
561   S., Javorniczky, J., and Krummel, P.: The Antarctic ozone hole during 2010, Aust. Meteorol. Ocean.
562   Journal., 61, 253, 2011.

563   Kravitz, B., and Robock, A.: Climate effects of high-latitude volcanic eruptions: Role of the time of
564   year, J. Geophys. Res. Atmos., 116, D01105, 10.1029/2010JD014448, 2011.

565   Kunz, A., Konopka, P., Müller, R., and Pan, L. L.: Dynamical tropopause based on isentropic potential
566   vorticity gradients, J. Geophys. Res. Atmos., 116, D01110, doi: 10.1029/2010JD014343, 2011a.

567   Kunz, A., Pan, L. L., Konopka, P., Kinnison, D. E., and Tilmes, S.: Chemical and dynamical
568   discontinuity at the extratropical tropopause based on START08 and WACCM analyses, J. Geophys.
569   Res. Atmos., 116, D24302, doi: 10.1029/2011JD016686, 2011b.

570   Kunz, A., Sprenger, M., and Wernli, H.: Climatology of potential vorticity streamers and associated
571   isentropic transport pathways across PV gradient barriers, J. Geophys. Res. Atmos., 120, 3802-3821,
572   doi: 10.1002/2014jd022615, 2015.

573   Liu, Y. S., Fueglistaler, S., and Haynes, P. H.: Advection-condensation paradigm for stratospheric water
574   vapor, J. Geophys. Res. Atmos., 115, D24307, doi: 10.1029/2010JD014352, 2010.

575   Mazzera, D. M., Lowenthal, D. H., Chow, J. C., and Watson, J. G.: Sources of PM10 and sulfate aerosol
576   at McMurdo station, Antarctica, Chemosphere, 45, 347-356, doi:
577   https://doi.org/10.1016/S0045-6535(00)00591-9, 2001.

578   Niemeier, U., and Schmidt, H.: Changing transport processes in the stratosphere by radiative heating of
579   sulfate aerosols, Atmos. Chem. Phys., 17, 14871-14886, doi: 10.5194/acp-17-14871-2017, 2017.

580   Olsen, M. A., Douglass, A. R., Schoeberl, M. R., Rodriquez, J. M., and Yoshida, Y.: Interannual
581   variability of ozone in the winter lower stratosphere and the relationship to lamina and irreversible
582   transport, J. Geophys. Res.-Atmos., 115, 10.1029/2009jd013004, 2010.

583   O'Sullivan, D., and Dunkerton, T. J.: The influence of the quasi-biennial oscillation on global
584   constituent distributions, J. Geophys. Res. Atmos., 102, 21731-21743, doi: 10.1029/97JD01689,
585   1997.

586   Palazzi, E., Fierli, F., Stiller, G. P., and Urban, J.: Probability density functions of long-lived tracer
587   observations from satellite in the subtropical barrier region: data intercomparison, Atmos. Chem.
588   Phys., 11, 10579-10598, doi: 10.5194/acp-11-10579-2011, 2011.

589   Pallister, J. S., Schneider, D. J., Griswold, J. P., Keeler, R. H., Burton, W. C., Noyles, C., Newhall, C.
590   G., and Ratdomopurbo, A.: Merapi 2010 eruption—Chronology and extrusion rates monitored with
591   satellite radar and used in eruption forecasting, J. Volcanol. Geotherm. Res., 261, 144-152, doi:
592   http://dx.doi.org/10.1016/j.jvolgeores.2012.07.012, 2013.

Atmospheric
Chemistry
and Physics
Discussions

593   Pausata, F. S. R., Chafik, L., Caballero, R., and Battisti, D. S.: Impacts of high-latitude volcanic
594   eruptions on ENSO and Asian monsoon, Proceedings of the National Academy of Sciences, 112,
595   13784-13788, doi: 10.1073/pnas.1509153112, 2015.
596   Ploeger, F., Konopka, P., Gunther, G., Grooss, J. U., and Muller, R.: Impact of the vertical velocity
597   scheme on modeling transport in the tropical tropopause layer, J. Geophys. Res. Atmos., 115, 14, doi:
598   10.1029/2009jd012023, 2010.
599   Ploeger, F., Fueglistaler, S., Grooss, J. U., Gunther, G., Konopka, P., Liu, Y. S., Muller, R., Ravegnani,
600   F., Schiller, C., Ulanovski, A., and Riese, M.: Insight from ozone and water vapour on transport in
601   the tropical tropopause layer (TTL), Atmos. Chem. Phys., 11, 407-419, doi:
602   10.5194/acp-11-407-2011, 2011.
603   Rößler, T., Stein, O., Heng, Y., and Hoffmann, L.: Regional and seasonal truncation errors of trajectory
604   calculations using ECMWF high-resolution operational analyses and forecasts, Geosci. Model Dev.
605   Discuss., 2017, 1-27, doi: 10.5194/gmd-2016-314, 2017.
606   Sand, M., Samset, B. H., Balkanski, Y., Bauer, S., Bellouin, N., Berntsen, T. K., Bian, H., Chin, M.,
607   Diehl, T., Easter, R., Ghan, S. J., Iversen, T., Kirkevåg, A., Lamarque, J. F., Lin, G., Liu, X., Luo, G.,
608   Myhre, G., Noije, T. V., Penner, J. E., Schulz, M., Seland, Ø., Skeie, R. B., Stier, P., Takemura, T.,
609   Tsigaridis, K., Yu, F., Zhang, K., and Zhang, H.: Aerosols at the poles: an AeroCom Phase II
610   multi-model evaluation, Atmos. Chem. Phys., 17, 12197-12218, doi: 10.5194/acp-17-12197-2017,
611   2017.
612   Schoeberl, M. R., Douglass, A. R., Zhu, Z. X., and Pawson, S.: A comparison of the lower stratospheric
613   age spectra derived from a general circulation model and two data assimilation systems, J. Geophys.
614   Res. Atmos., 108, 16, doi: 10.1029/2002jd002652, 2003.
615   Shuckburgh, E., Norton, W., Iwi, A., and Haynes, P.: Influence of the quasi-biennial oscillation on
616   isentropic transport and mixing in the tropics and subtropics, J. Geophys. Res. Atmos., 106,
617   14327-14337, doi: 10.1029/2000JD900664, 2001.
618   Sigl, M., Winstrup, M., McConnell, J. R., Welten, K. C., Plunkett, G., Ludlow, F., Buntgen, U., Caffee,
619   M., Chellman, N., Dahl-Jensen, D., Fischer, H., Kipfstuhl, S., Kostick, C., Maselli, O. J., Mekhaldi,
620   F., Mulvaney, R., Muscheler, R., Pasteris, D. R., Pilcher, J. R., Salzer, M., Schupbach, S., Steffensen,
621   J. P., Vinther, B. M., and Woodruff, T. E.: Timing and climate forcing of volcanic eruptions for the
622   past 2,500 years, Nature, 523, 543-549, doi:
623   10.1038/nature14565http://www.nature.com/nature/journal/v523/n7562/abs/nature14565.html#suppl
624   ementary-information, 2015.
625   Solomon, S.: Stratospheric ozone depletion: A review of concepts and history, Reviews of Geophysics,
626   37, 275-316, doi: 10.1029/1999RG900008, 1999.
627   Solomon, S., Daniel, J. S., Neely, R. R., Vernier, J.-P., Dutton, E. G., and Thomason, L. W.: The
628   Persistently Variable "Background" Stratospheric Aerosol Layer and Global Climate Change,
629   Science, 333, 866-870, doi: 10.1126/science.1206027, 2011.
630   Solomon, S., Ivy, D. J., Kinnison, D., Mills, M. J., Neely, R. R., and Schmidt, A.: Emergence of healing
631   in the Antarctic ozone layer, Science, doi: 10.1126/science.aae0061, 2016.
632   Solomon, S., Sanders, R. W., Garcia, R. R., and Keys, J. G.: Increased chlorine dioxide over Antarctica
633   caused by volcanic aerosols from Mount-Pinatubo, Nature, 363, 245–248, doi:
634   https://doi.org/10.1038/363245a0, 1993.
635   Stohl, A., Forster, C., Frank, A., Seibert, P., and Wotawa, G.: Technical note: The Lagrangian particle
636   dispersion model FLEXPART version 6.2, Atmos. Chem. Phys., 5, 2461-2474,
637   doi:10.5194/acp-5-2461-2005, 2005.
638   Stone, K. A., Solomon, S., Kinnison, D. E., Pitts, M. C., Poole, L. R., Mills, M. J., Schmidt, A., Neely,
639   R. R., Ivy, D., Schwartz, M. J., Vernier, J.-P., Johnson, B. J., Tully, M. B., Klekociuk, A. R.,

Atmospheric
Chemistry
and Physics
Discussions

640 König-Langlo, G., and Hagiya, S.: Observing the Impact of Calbuco Volcanic Aerosols on South
641 Polar Ozone Depletion in 2015, J. Geophys. Res. Atmos., 122, 11,862-811,879, doi:
642 10.1002/2017JD026987, 2017.
643 Surono, Jousset, P., Pallister, J., Boichu, M., Buongiorno, M. F., Budisantoso, A., Costa, F., Andreastuti,
644 S., Prata, F., Schneider, D., Clarisse, L., Humaida, H., Sumarti, S., Bignami, C., Griswold, J., Carn,
645 S., Oppenheimer, C., and Lavigne, F.: The 2010 explosive eruption of Java's Merapi volcano—A
646 '100-year' event, J. Volcanol. Geotherm. Res., 241, 121-135, doi:
647 http://dx.doi.org/10.1016/j.jvolgeores.2012.06.018, 2012.
648 Tilmes, S., Muller, R., and Salawitch, R.: The sensitivity of polar ozone depletion to proposed
649 geoengineering schemes, Science, 320, 1201-1204, doi: 10.1126/science.1153966, 2008.
650 Vernier, J. P., Thomason, L. W., Pommereau, J. P., Bourassa, A., Pelon, J., Garnier, A., Hauchecorne,
651 A., Blanot, L., Trepte, C., Degenstein, D., and Vargas, F.: Major influence of tropical volcanic
652 eruptions on the stratospheric aerosol layer during the last decade, Geophys. Res. Lett., 38, L12807,
653 10.1029/2011GL047563, 2011.
654 Vogel, B., Pan, L. L., Konopka, P., Gunther, G., Muller, R., Hall, W., Campos, T., Pollack, I.,
655 Weinheimer, A., Wei, J., Atlas, E. L., and Bowman, K. P.: Transport pathways and signatures of
656 mixing in the extratropical tropopause region derived from Lagrangian model simulations, J.
657 Geophys. Res.-Atmos., 116, 16, doi: 10.1029/2010jd014876, 2011.
658 von Glasow, R., Bobrowski, N., and Kern, C.: The effects of volcanic eruptions on atmospheric
659 chemistry, Chem. Geol., 263, 131-142, doi: http://dx.doi.org/10.1016/j.chemgeo.2008.08.020, 2009.
660 Watson, P. A. G., and Gray, L. J.: How Does the Quasi-Biennial Oscillation Affect the Stratospheric
661 Polar Vortex?, J. Atmos. Sci., 71, 391-409, doi: 10.1175/jas-d-13-096.1, 2014.
662 Wohltmann, I., and Rex, M.: Improvement of vertical and residual velocities in pressure or hybrid
663 sigma-pressure coordinates in analysis data in the stratosphere, Atmos. Chem. Phys., 8, 265-272, doi:
664 10.5194/acp-8-265-2008, 2008.
665 Wu, X., Griessbach, S., and Hoffmann, L.: Equatorward dispersion of a high-latitude volcanic plume
666 and its relation to the Asian summer monsoon: a case study of the Sarychev eruption in 2009, Atmos.
667 Chem. Phys., 17, 13439-13455, doi: 10.5194/acp-17-13439-2017, 2017.
668 Zuev, V. V., Zueva, N. E., Savelieva, E. S., and Gerasimov, V. V.: The Antarctic ozone depletion
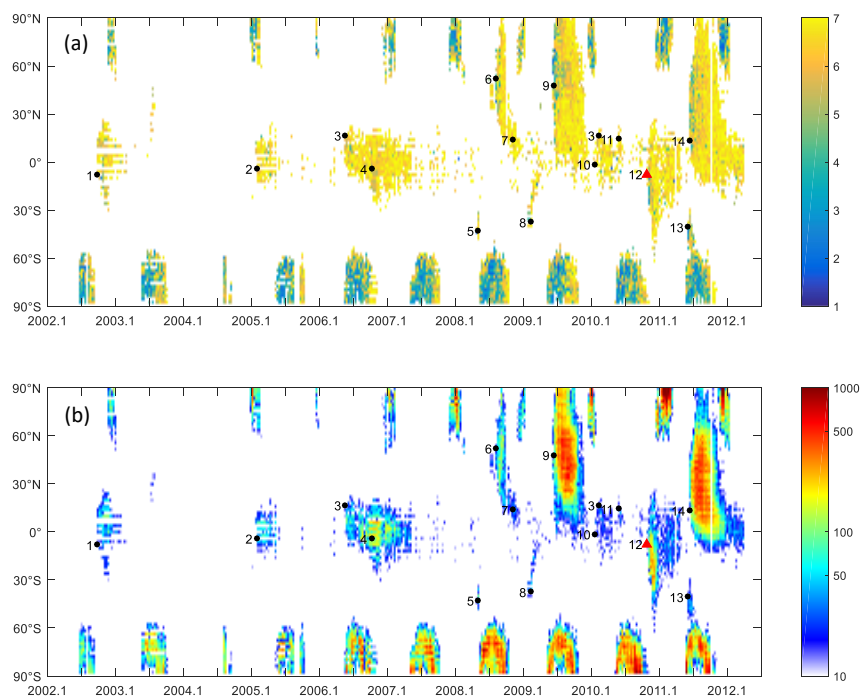669 caused by Erebus volcano gas emissions, Atmos. Environ., 122, 393-399, doi:
670 https://doi.org/10.1016/j.atmosenv.2015.10.005, 2015.

Figure 1: (a) Median value of ACI (ACI<7) and (b) number of MIPAS aerosol detections between 13 and 20 km (bin size 10 days and 2 ° in latitude). The red triangle indicates the eruption of Mount Merapi. The black dots indicate 1 Raung, 2 Manam, 3 Soufriere Hills, 4 Tavurvur (Rabaul), 5 Chaitén, 6 Kasatochi, 7 Dalaffilla, 8 Australian bushfire, 9 Sarychev Peak, 10 Nyamuragira, 11 Pacaya, 12 Mount Merapi, 13 Puyehue-Cordón Caulle, 14 Nabro.
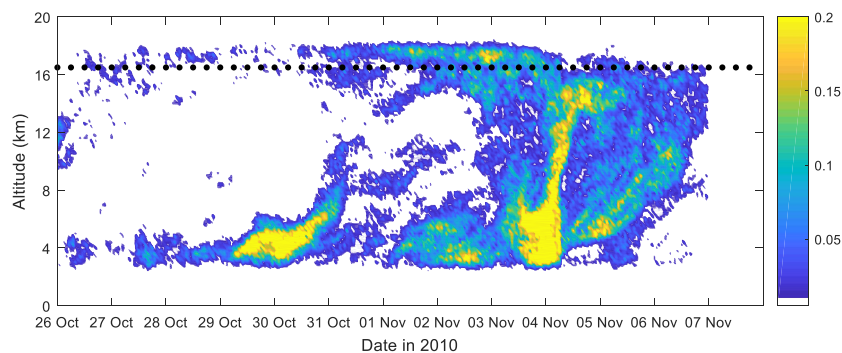
Figure 2: Merapi SO₂ emission time series (unit: kg m^{-1} s^{-1}) derived from AIRS measurements using a backward trajectory approach (see text for details). The emission data are binned every 1 h and 0.2 km. Gray dots denote the height of the thermal tropopause (based on the ERA–Interim reanalysis).
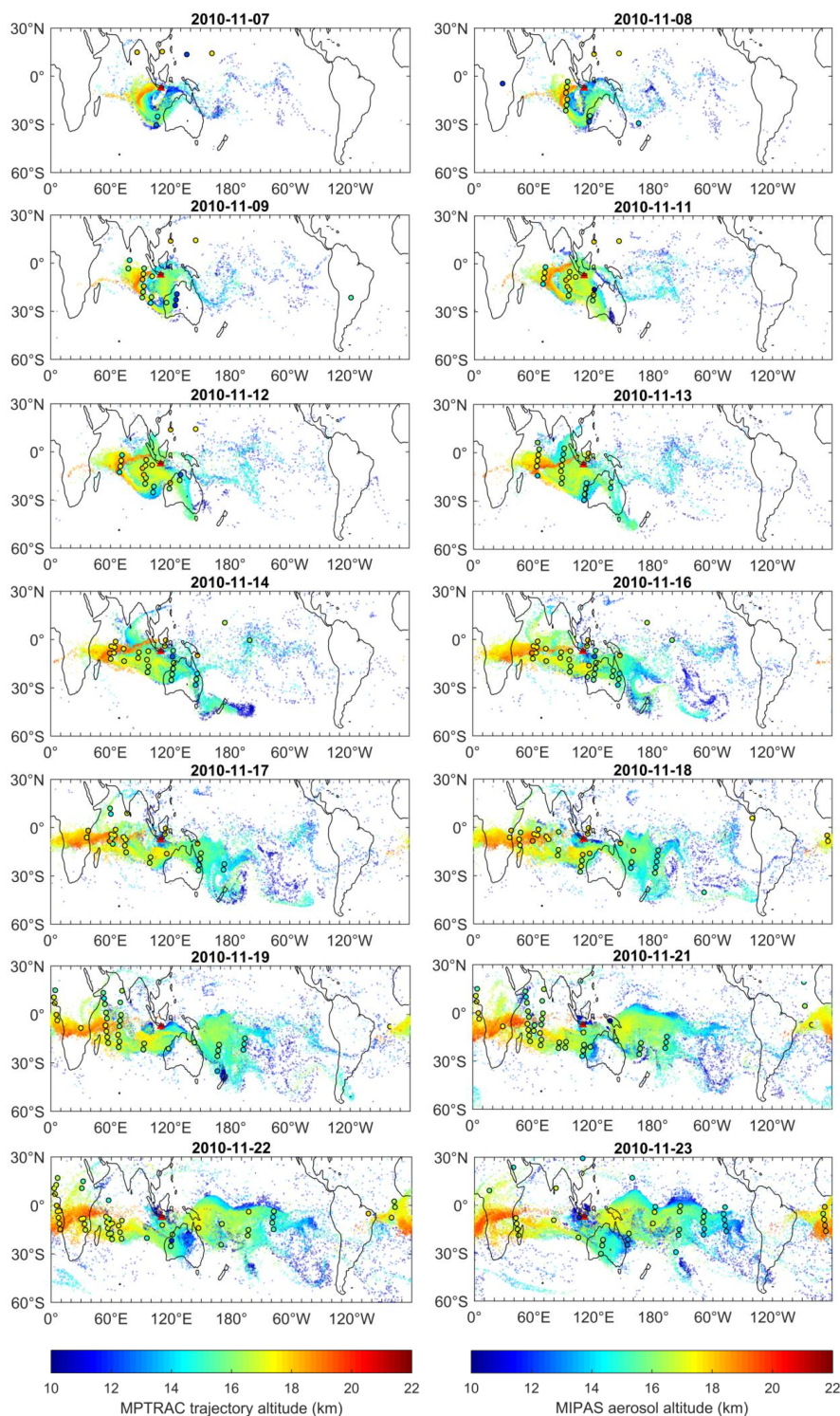
Figure 3: Distribution of the volcanic plume (showing only air parcels higher than 10 km, shading) from MPTRAC simulations (shown for 00:00UTC on selected days) and MIPAS aerosol detections (ACI < 7) within ±6 h (color-filled circles). The altitudes of all

air parcels, regardless of their SO_2 values, are shown. The red triangle denotes the location of Mount Merapi.
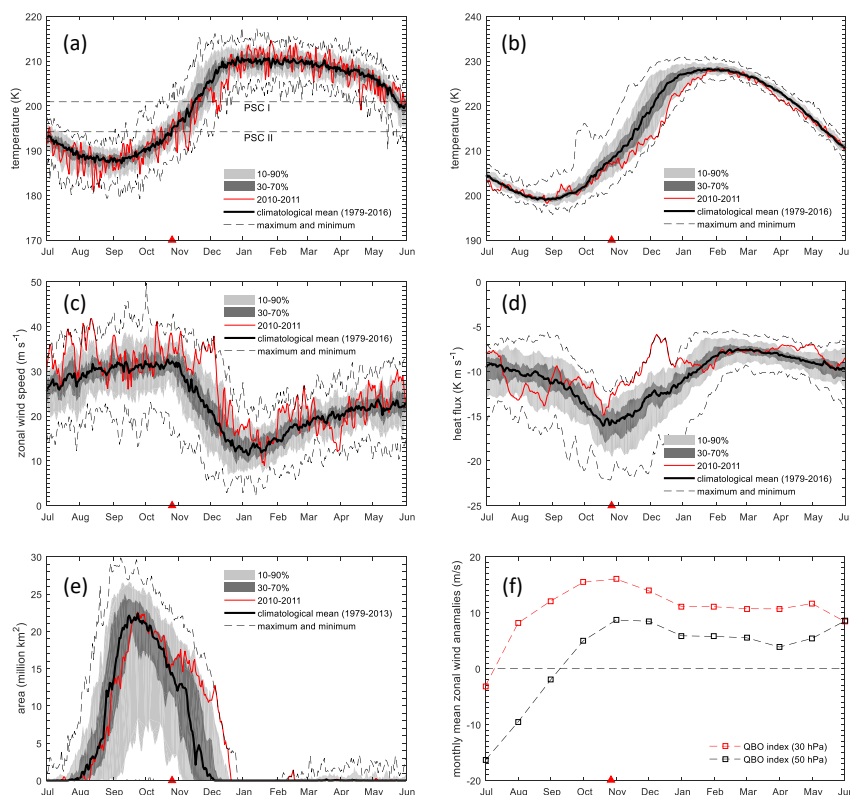
Figure 4: (a) Minimum temperature south of 50 °S at 150 hPa; (b) temperature averaged over the polar cap for latitudes south of 60 °S at 150 hPa; (c) zonal wind speed at 60 °S at 150 hPa; (d) eddy heat flux averaged between 45 °S and 75 °S for the 45-day period prior to the date indicated at 150 hPa; (e) ozone hole area from July 2010 to May 2011; (f) monthly mean zonal wind anomalies at 30 and 50 hPa. Temperatures for PSC existence in (a) are determined by assuming a nitric acid concentration of 6 ppbv and a water vapor concentration of 4.5 ppmv. (a)–(e) are based on MERRA2 data and (f) is based on NCEP/NCAR reanalysis. The ozone hole area in (e) is determined from OMI ozone satellite measurements. The red triangles indicate the time of the Merapi eruption.

Atmospheric
Chemistry
and Physics
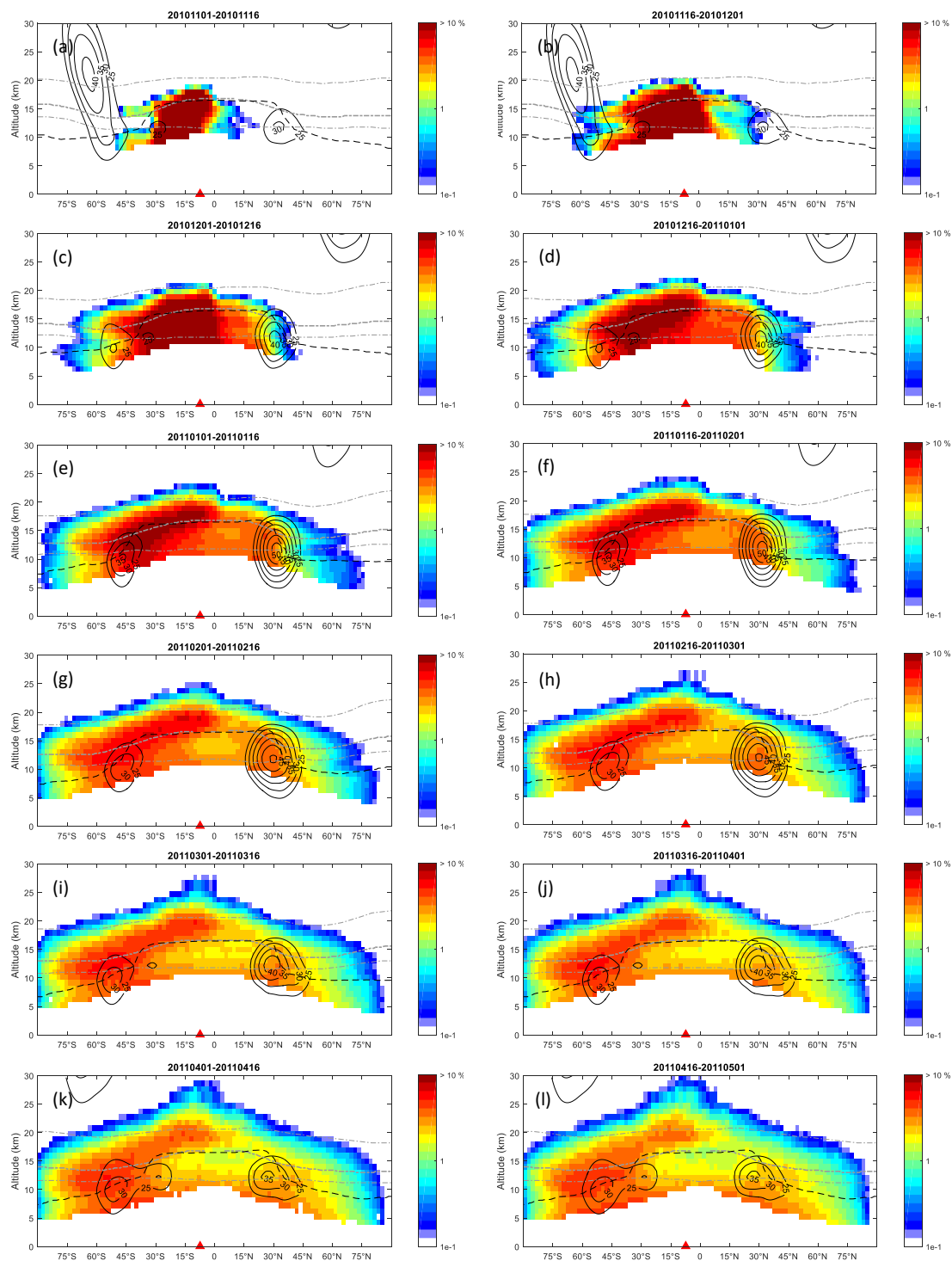Discussions

Open Access

EGU

Figure 5: Percentage (%) of air parcels in proportion to the total number of air parcels from MPTRAC simulations, overlapped with monthly mean zonal winds (black contours), the thermal tropopause (black dashed line), the 380 K potential temperature isoline (thick gray dashed line) and 350 and 480 K potential temperature isolines (thin gray dashed lines). Results

Atmospheric
Chemistry
and Physics
Discussions

Open Access

EGU

are binned every 2 ° in latitude and 1 km in altitude. The red triangle denotes the latitude of the Merapi. Please see title of each figure for the time period covered.
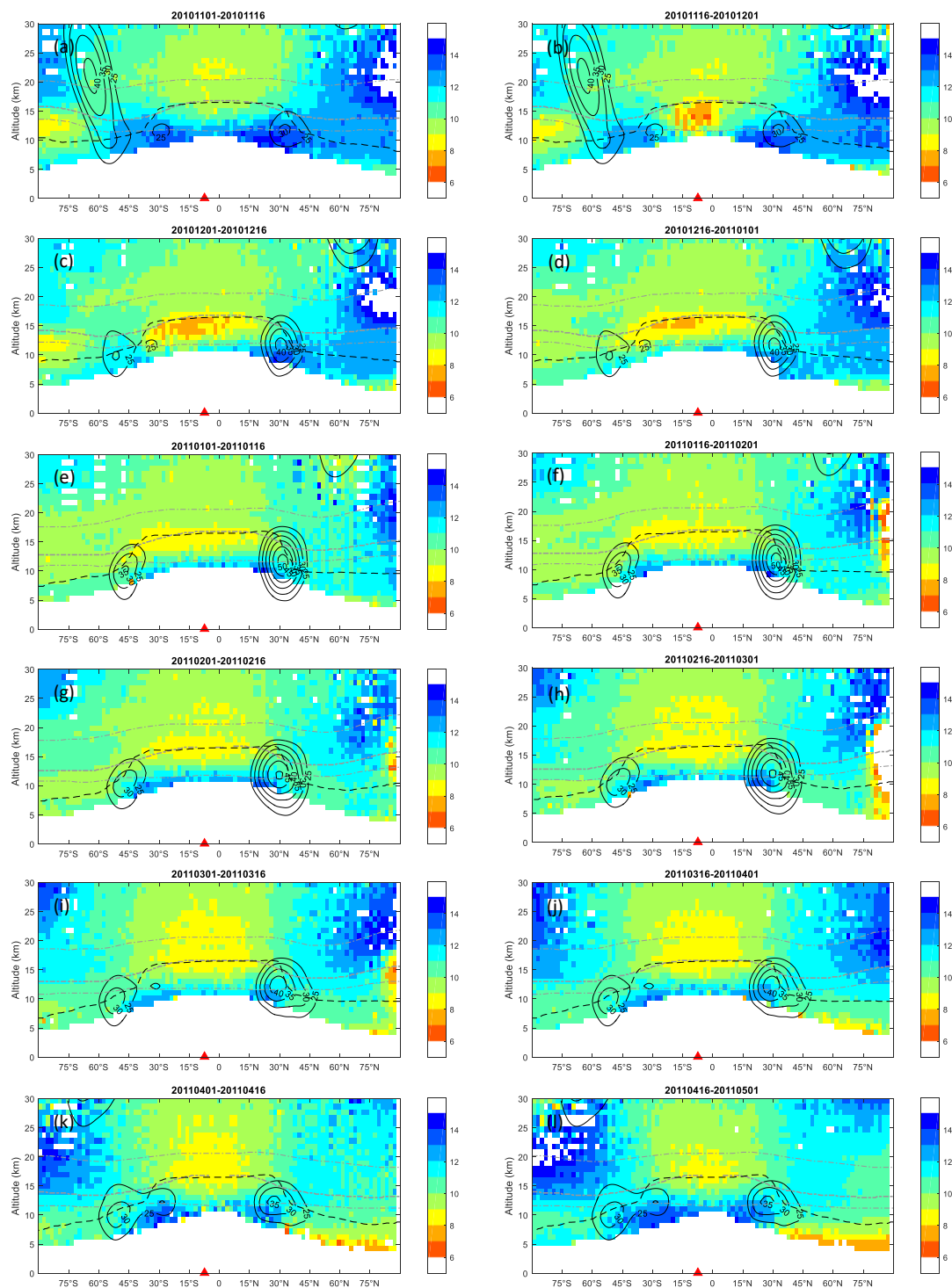
Figure 6: Median value of ACI of MIPAS aerosol detections (ice clouds filtered out), overlapped with monthly mean zonal winds (black contours), the thermal tropopause (black dashed line), the 380 K potential temperature isoline (thick gray dashed line) and 350 and 480 K potential temperature isolines (thin gray dashed lines). Results are binned

Atmospheric
Chemistry
and Physics
Discussions

Open Access

EGU

every 2 ° in latitude and 1 km in altitude. Only median ACI values of 5–15 are shown. The red triangle denotes the latitude of the Merapi. Please see title of each figure for the time period covered.
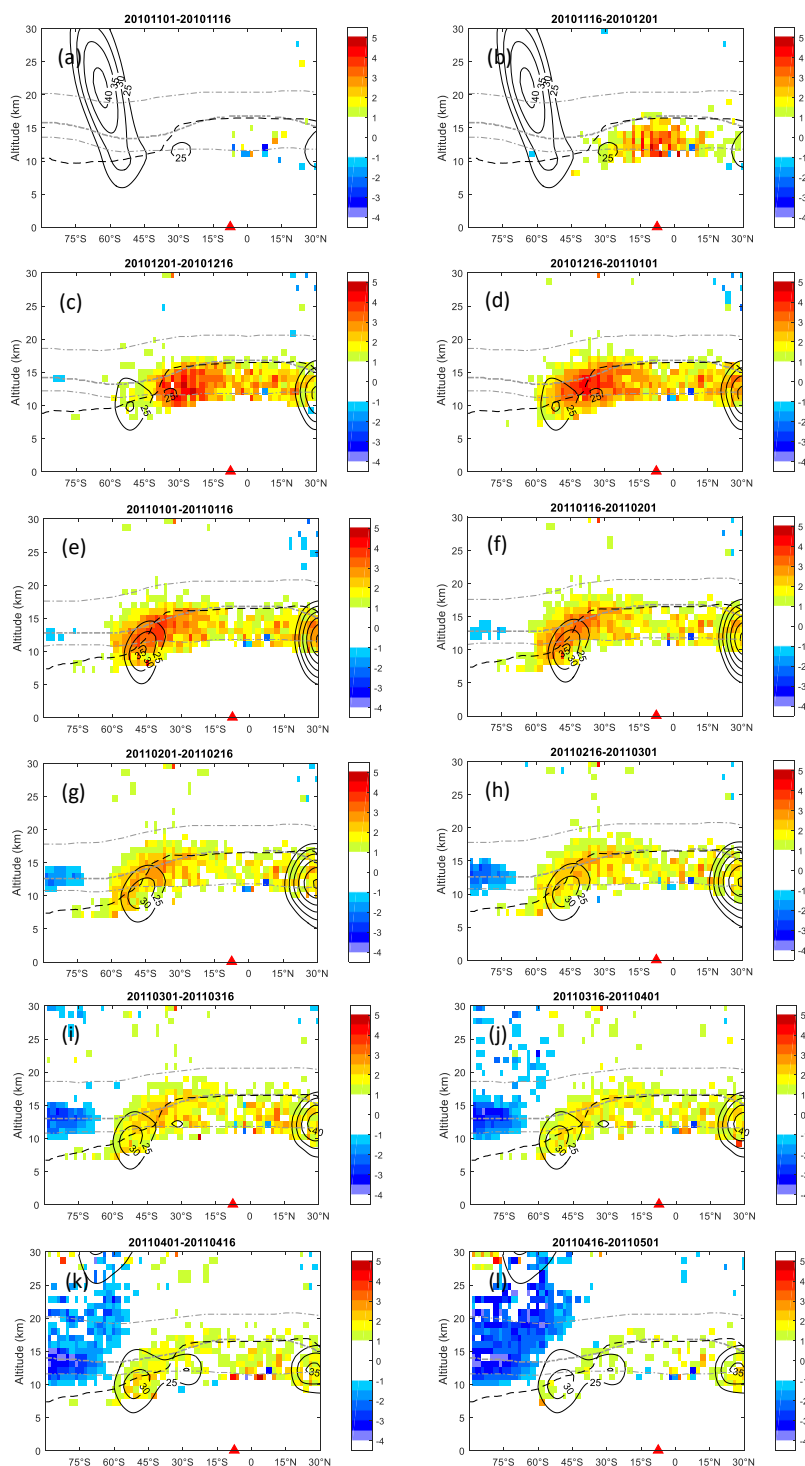
Atmospheric
Chemistry
and Physics
Discussions

Figure 7: Change of aerosol load after the eruption of Merapi in 2010, overlapped with monthly mean zonal winds (black contours), the thermal tropopause (black dashed line), the 380 K potential temperature isoline (thick gray dashed line) and 350 and 480 K potential temperature isolines (thin gray dashed lines). Results are binned every 2 ° in

Atmospheric
Chemistry
and Physics
Discussions

Open Access

latitude and 1 km in altitude. The red triangle denotes the latitude of the Merapi. Please see title of each figure for the time period covered.
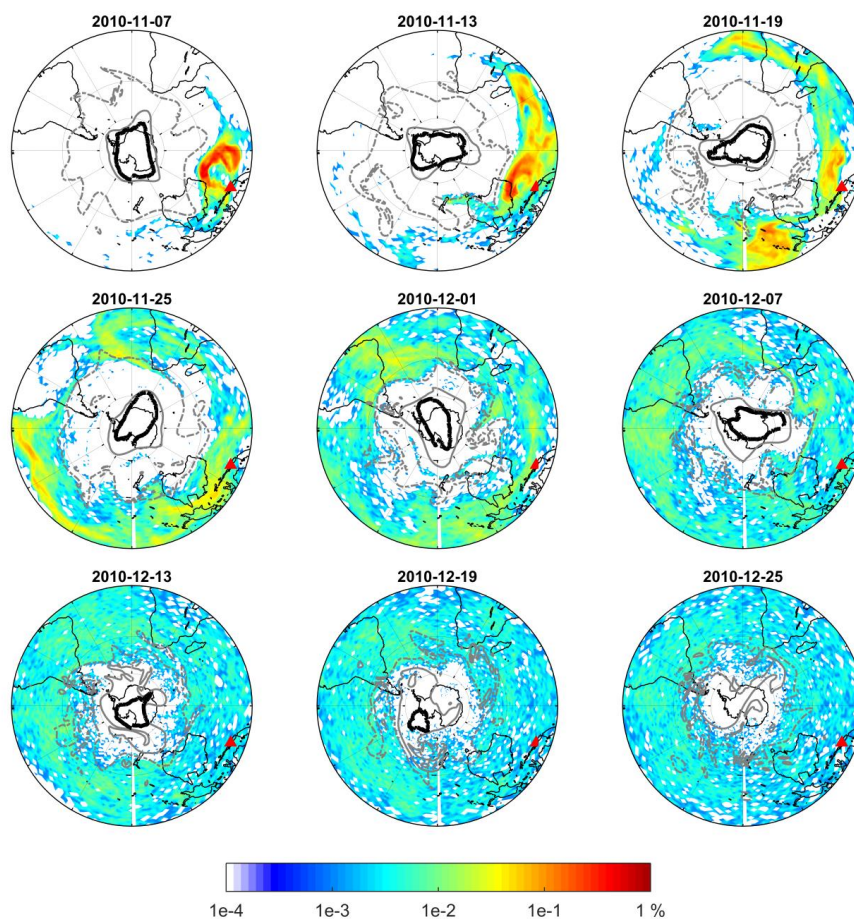
Figure 8: Percentage (%) of air parcels between the isentropic surfaces of 350 and 480 K in proportion to the total number of air parcels initialized in the Lagrangian transport simulation, at 12:00 UTC on selected dates. Results are binned every 2 ° in longitude and 1 ° in latitude. The black contour indicates OMI daily mean ozone column density of 220 DU. PV contours marked with gray dashed and solid lines show transport boundaries on the 350 and 480 K isentropic surfaces respectively (Kunz et al., 2015). The red triangle denotes the location of Mount Merapi
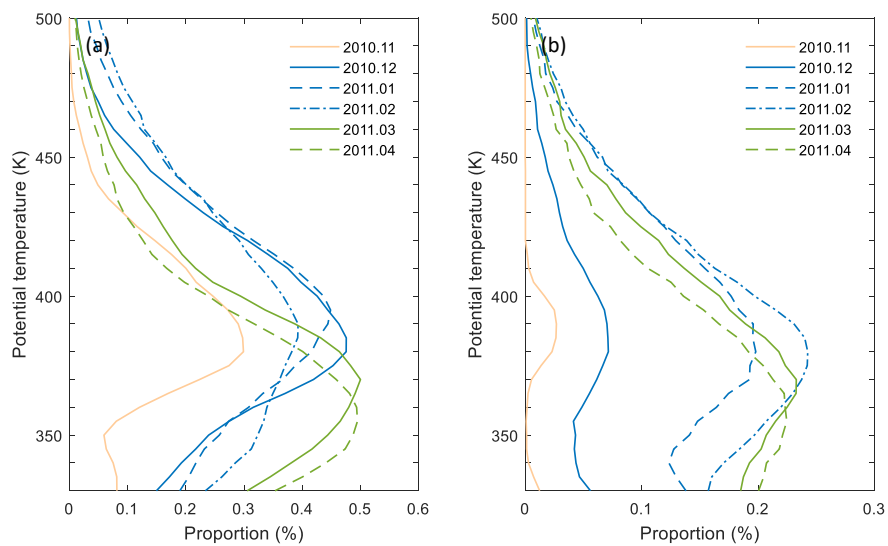
Figure 9: (a) Proportion (%) of the air parcels poleward of the PV-based transport boundaries at the end of each month; (b) proportion (%) of the air parcels south of 60 ˚S.
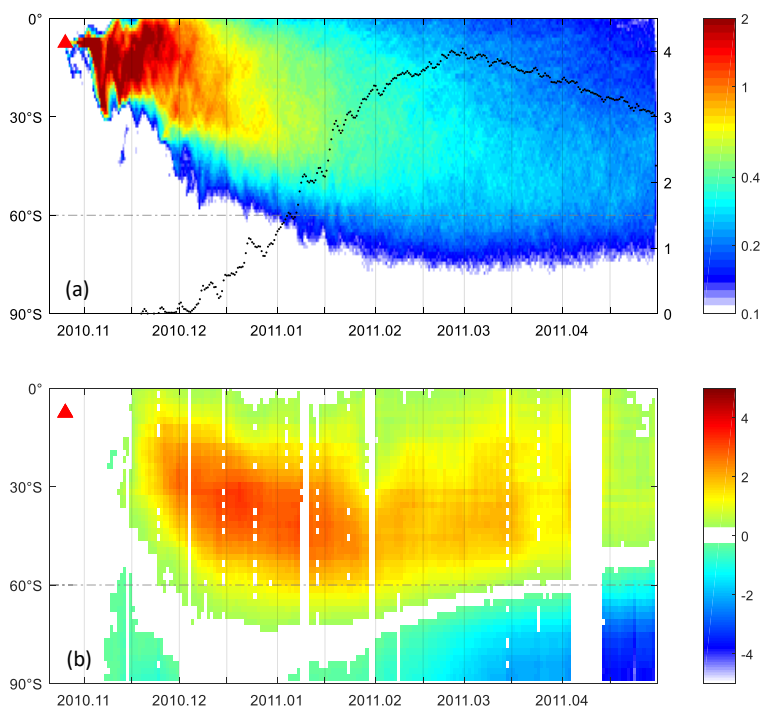
Figure 10: (a) Percentage (%) of air parcels between 350 and 480 K from MPTRAC simulations (shading, only percentages larger than 0.1% are shown; bin size: 12h and 1 ° in latitude), overlapped with proportion (%) of air parcels south of 60 °S (black dots); (b) Change of measured aerosol load between 350 and 480 K. Positive/negative values indicate increase/decrease of aerosol (bin size: 24h and 1 °in latitude). The red triangle denotes the time and latitude of the Merapi eruption